Article

TRANSPARENT PROCESS

THE EMBO JOURNAL

Centriole translocation and degeneration during ciliogenesis in *Caenorhabditis elegans* neurons

Wenjing Li, Peishan Yi, Zhiwen Zhu, Xianliang Zhang, Wei Li & Guangshuo Ou*

Abstract

Neuronal cilia that are formed at the dendritic endings of sensory neurons are essential for sensory perception. However, it remains unclear how the centriole-derived basal body is positioned to form a template for cilium formation. Using fluorescence time-lapse microscopy, we show that the centriole translocates from the cell body to the dendrite tip in the *Caenorhabditis elegans* sensory neurons. The centriolar protein SAS-5 interacts with the dynein light-chain LC8 and conditional mutations of cytoplasmic dynein-1 block centriole translocation and ciliogenesis. The components of the central tube are essential for the biogenesis of centrioles, which later drive ciliogenesis in the dendrite; however, the centriole loses these components at the late stage of centriole translocation and subsequently recruits transition zone and intraflagellar transport proteins. Together, our results provide a comprehensive model of ciliogenesis in sensory neurons and reveal the importance of the dynein-dependent centriole translocation in this process.

Keywords centriole; dendritic transport; dynein; neuronal ciliogenesis
Subject Categories Cell Adhesion, Polarity & Cytoskeleton; Membrane & Intracellular Transport
DOI 10.15252/embj.201796883 | Received 6 March 2017 | Revised 6 June 2017 | Accepted 3 July 2017 | Published online 25 July 2017
The EMBO Journal (2017) 36: 2553–2566

Introduction

Our perceptions of the natural world originate from our senses of an unending variety of stimuli in the environment. Sensory organs have developed specialized structures to perform this feat. For example, the mammalian olfactory system is optimized for the detection and discrimination of odorant molecules through odorant receptor proteins that are expressed by peripheral olfactory sensory neurons (OSNs; McEwen *et al*, 2008; Challis *et al*, 2015). A bipolar OSN possesses an unbranched axon that projects to the olfactory bulb and a dendrite that extends apically and terminates in a dendritic knob at the epithelial surface. A remarkable feature of OSNs is the formation of olfactory cilia that emanate from the dendritic knob and project into the mucus of the nasal cavity (Menco, 1997; Jenkins *et al*, 2009). These cilia harbor G-protein-coupled receptors and other proteins that are essential for olfactory signal perception and transduction, making them the sites where the detection of a chemical odor is converted into an electrical response (Berbari *et al*, 2008). Importantly, each dendritic knob contains 10–30 olfactory cilia of up to 50–60 μm in length, which increases the sensory surface of the ciliated epithelium to amplify the ability of odorant detection (Cuschieri & Bannister, 1975a; Mashukova *et al*, 2006; Oberland & Neuhaus, 2014). Disruption of ciliary structure or function causes human ciliopathies such as anosmia (inability to perceive odors) or dysosmia (altered odor perception), highlighting the significance of olfactory cilia in odor perception (Toller, 1999; Klysik, 2008; Brown & Witman, 2014).

Cilia are microtubule-based organelles in which the ninefold symmetric array of doublet axonemal microtubules is extended from the centriole-derived basal body (Ward *et al*, 1975; Pedersen *et al*, 2008; Reiter *et al*, 2012). The assembly of olfactory cilia has unique features, as multiple cilia are present at the dendritic ending of an OSN (Menco, 1980; Challis *et al*, 2015; Falk *et al*, 2015). Cells normally use one centriole to build a single cilium. The multiciliated OSNs are thought to multiply their centrioles in the cell body, and then the centrioles undergo long distance dendritic transport to arrive at the dendritic knob, where they permit the elongation of cilia (Dirksen, 1974; Schwarzenbacher *et al*, 2005). Immunohistochemistry on ciliogenesis in OSNs has outlined the possible cellular events involved, including dendrite outgrowth, centriole amplification and translocation, and cilium formation (Fig EV1A; Hagiwara *et al*, 2004; Jenkins *et al*, 2009). However, the dynamic behavior of centriole and the underlying molecular regulation remain largely unexplored due to the complex developmental processes (at approximately E10–E14 in mouse) and the lack of an experimental methodology for live cell microscopy (Cuschieri & Bannister, 1975a,b; Hagiwara *et al*, 2004; Jenkins *et al*, 2009).

The nematode *Caenorhabditis elegans* offers a compelling model system to explore de novo ciliogenesis in the nervous system. All 60 ciliated cells in an adult *C. elegans* hermaphrodite are sensory neurons (Ward *et al*, 1975; Ware *et al*, 1975; Perkins *et al*, 1986; Inglis *et al*, 2007; Doroquez *et al*, 2014). In *C. elegans* embryos, previous live imaging studies have shown that sensory dendrites in amphids extend from the cell body via retrograde elongation, such that the growing dendrite is anchored at the presumptive nose while the soma translocates toward the posterior (Sulston *et al*, 1983;

Tsinghua-Peking Center for Life Sciences, School of Life Sciences and MOE Key Laboratory for Protein Science, Tsinghua University, Beijing, China
*Corresponding author. Tel: +86 10 62794766; E-mail: guangshuoou@tsinghua.edu.cn

Heiman & Shaham, 2009; Schouteden *et al*, 2015). As a result, the basal bodies in these neurons do not undergo the dendritic translocation but are initially positioned at dendrite tips where sensory cilia emerge (Perkins *et al*, 1986; Heiman & Shaham, 2009). However, in mammalian OSNs, centrioles were detected in the middle of emerging dendrites and then arrived at the dendrite tips in mature neurons (Ying *et al*, 2014), which suggests that centriole translocation is an early step before the assembly of olfactory cilia (Cuschieri & Bannister, 1975a). Moreover, cilium formation in the *C. elegans* PQR sensory neuron may share similarities with ciliogenesis in mammalian OSNs (Figs 1A and EV1A). During the first larval stage, PQR is generated by asymmetric cell divisions of the QL neuroblast; after migration, PQR elongates its dendrite and constructs a sensory cilium at its dendrite ending (Sulston & Horvitz, 1977; Perkins *et al*, 1986). We have developed fluorescence time-lapse microscopy to document Q neuroblast division, migration, and dendrite outgrowth in live *C. elegans* larvae (Chai *et al*, 2012).

Here, we use the live imaging protocol, for the first time, to define the subcellular events involved in the formation of a sensory cilium of the *C. elegans* PQR neuron. We document centriole translocation from the cell body toward the dendrite tip when the dendrite elongates. Using biochemical and genetic approaches, we find that centriole translocation depends on cytoplasmic dynein-1 and that the centriolar protein SAS-5 interacts with the dynein light-chain LC8. We further document the sequential accumulation of transition zone proteins and intraflagellar transport (IFT) proteins during the late stage of centriole translocation. Unexpectedly, centriolar proteins are removed upon the accumulation of transition zone proteins. Taken together, our results establish a comprehensive model of the de novo cilium formation in sensory neurons and provide insights into the same process in the mammalian olfactory system.

Results

Centriole translocation and degeneration in the dendrite

To monitor the dynamic behavior of centriole during ciliogenesis in *C. elegans* neurons, we labeled the components of the centriole core proteins including SAS-4, SAS-5, and SAS-6 with a fluorescent protein (Leidel & Gonczy, 2003; Delattre *et al*, 2004; Leidel *et al*, 2005). Using a CRISPR-Cas9-assisted homologous recombination method, we constructed a mMaple3::SAS-4 knock-in (KI) strain. The fluorescence protein mMaple3 marks the tagged protein with green fluorescence (Wang *et al*, 2014). The KI animal is indistinguishable from the wild-type (WT) nematodes in animal development. The particle bombardment transformation protocol (Praitis *et al*, 2001) was previously used to generate an integrant low-copy GFP::SAS-5 or SAS-6::GFP strain. As illustrated in the early studies, these markers label centrioles during *C. elegans* development (Cabral *et al*, 2013); for example, the GFP fluorescence of SAS-6::GFP was detected as a single spot at the spindle pole during Q cell asymmetric division and split to double spots (Fig EV1B). To visualize the PQR sensory neuron, we expressed mCherry-tagged histone and plasma membrane proteins under the control of the Q neuroblast-specific promoter P*egl-17* (Figs 1B and EV1B; Ou *et al*, 2010).

To define the subcellular localization of the centriole during PQR development in live *C. elegans* larvae, we performed fluorescence time-lapse microscopy of the developing larvae at 2-min intervals over a period of 2–3 h. Our recordings usually start when the cell body of PQR arrives at the destination, while the leading edge continues to elongate to form the dendrite (Fig 1B). The dendrite grows out first, and the centriole translocation follows dendritic extension (Fig 1B). Time 0 refers to the start point of the leading edge extension from the non-motile cell body. At approximately 15 min, one centriole moved into the growing dendrite, whereas the other remained immobile in the soma (Fig 1B and C, Movie EV1 and more examples in Fig EV2B). Quantification of the time-lapse movies showed that the motile centriole translocated for 67 ± 22 min for a total distance of 5.1 ± 2.7 μm (Mean ± SD; $N = 31$). These results provide direct evidence in live animals that the centriole undergoes dendritic translocation to build the sensory cilium.

Intriguingly, we found that the SAS-6::GFP fluorescence of the motile centriole disappeared in the growing dendrite at the late stage of centriole translocation. A gradual decrease in SAS-6::GFP fluorescence always occurred within 8 ± 2 min at 67 ± 22 min after the dendritic growth initiates, at the position of 5.1 ± 2.7 μm away from the cell body (Mean ± SD; $N = 6$; the representative images are shown in Figs 1D and EV2C), which suggests that the centriolar protein degradation may be programmed and argues against the possibility that they simply move out-of-focus during time-lapse recording. We showed that the SAS-6::GFP fluorescence from the non-motile centriole in the cell body did not change during our recording and that the dendritic growth appeared to be normal (Figs 1B and EV1B), excluding the possibility that the loss of SAS-6::GFP in the dendrite was caused by photo-bleaching or phototoxicity. Other centriole markers including mMaple3::SAS-4 could not be detected from the motile centriole in the dendrite but retained at the non-motile centriole in the cell body (Fig EV1C). Consistently, all these centriolar proteins disappeared from the base of cilia of other sensory neurons in the *C. elegans* amphid and phasmid (Fig 1E). Thus, our live imaging data indicate that centriolar proteins are lost from the motile centriole in the growing dendrite and support the previous observation that the *C. elegans* centriole generally degenerates (Perkins *et al*, 1986; Dammermann *et al*, 2009; Williams *et al*, 2011).

Centriolar proteins are essential for ciliogenesis in *Caenorhabditis elegans* neurons

It is well established that the centriole-derived basal body provides a template for nucleating axonemes. However, *C. elegans* centrioles do not have a cartwheel at their core but rather a central tube (O'Toole *et al*, 2003; Pelletier *et al*, 2006); and the early loss of the core centriolar proteins was detected in the developing dendrite (Fig 1D). We sought to rigorously examine the function of the centriolar protein SAS-4, SAS-5, and SAS-6 during ciliogenesis in *C. elegans* sensory neurons. To bypass the crucial function of centriolar proteins in cell division and embryonic development, we used the somatic CRISPR-Cas9 technique to generate conditional mutants of centriolar proteins in *C. elegans* L1 larvae (Fig 2A). We devised this technique to study the embryonically essential genes in Q cell division and migration (Shen *et al*, 2014). Using the same platform,

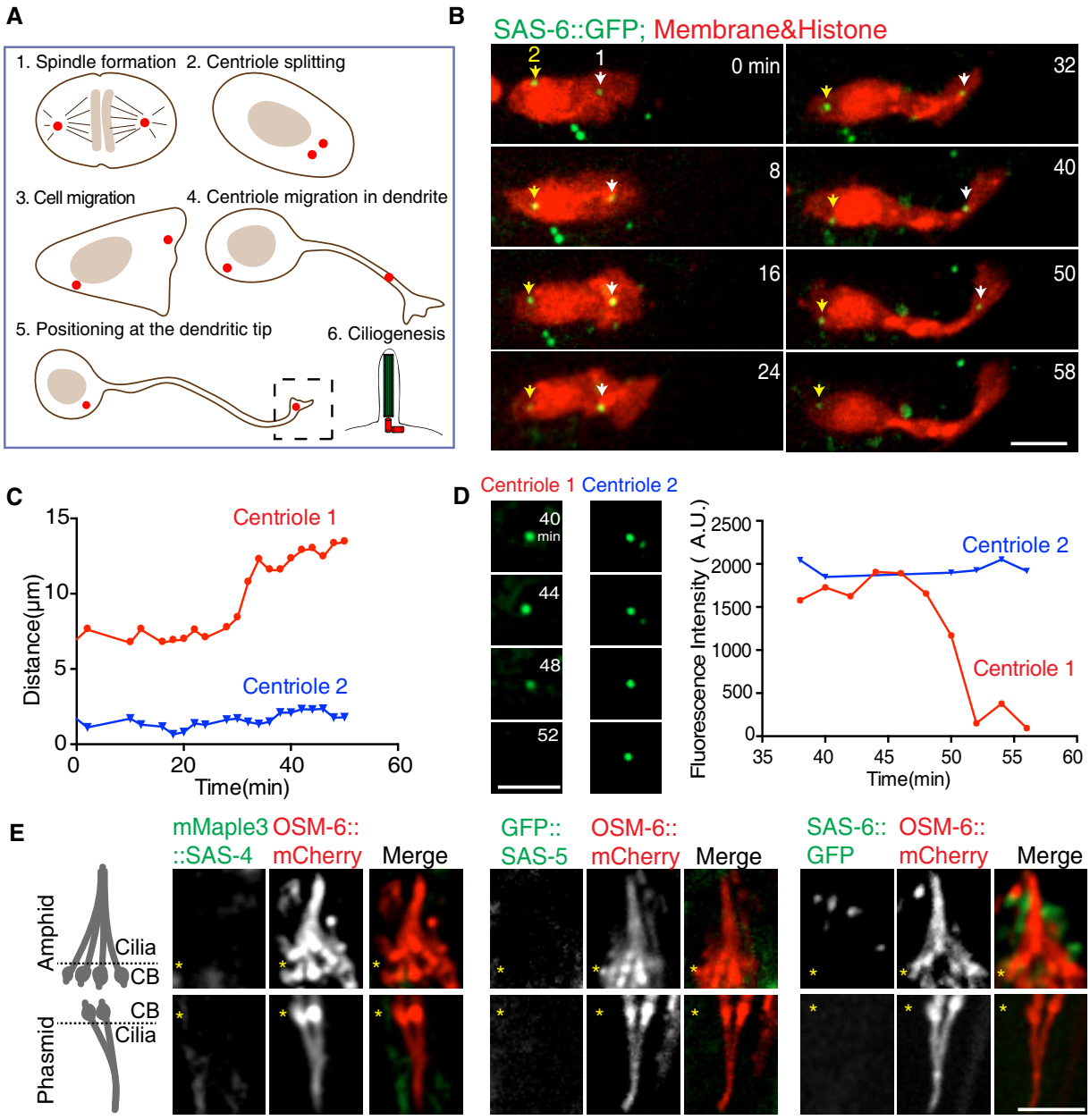

Figure 1. Centriole migration and degeneration in the dendrite.

A Schematics of the centriole positioning during ciliogenesis in Q neuroblast in *Caenorhabditis elegans*. Centriole translocates to the dendrite tip to initiate cilium assembly.

B, C (B) Representative fluorescence time-lapse images of the dynamic positioning of centrioles (green, labeled with SAS-6::GFP) and the plasma membrane/chromosomes (red, labeled with mCherry) during ciliogenesis. Time 0 refers to when the leading edge starts to extend from the non-motile cell body to form the dendrite, and the centriole migrates along with dendrite elongation. Note that centriole (1) translocates, whereas centriole (2) stays in the soma, and the centriole displacement defined by the position relative to cell body over time is quantified in (C) (Movie EV1). For details of the quantification, see methods and Fig EV2A; more examples are shown in Fig EV2B.

D At the end of centriole migration, the centriole signal gradually decreases (left). Individual fluorescent centrioles were tracked, and intensity was quantified over time (right). More examples are shown in Fig EV2C.

E No fluorescence of SAS-4, SAS-5, or SAS-6 was detected at the base of the cilia in *C. elegans* sensory neurons in adult worms. CB, ciliary base, indicated with yellow asterisks.

Data information: Scale bars, 5 μm.

we expressed the Cas9 endonuclease under the control of a heat-shock-inducible promoter to generate conditional mutants of *sas-4*, *sas-5*, and *sas-6* (Fig 2A and B). After heat-shock induction of Cas9 expression, T7 endonuclease I (T7EI)-based assays demonstrated that DNA fragments from *sas-4,-5,-6-sg* strains (*-sg* for the conditional mutant) were digested into two small fragments of the

expected sizes with the indels (insertion–deletion) of 9, 7, and 5%, respectively (Fig 2C). The conditional mutant embryos but not WT embryos exhibited embryonic lethality with the penetrance of 81 ± 4% (*sas-4-sg*), 94 ± 4% (*sas-5-sg*), and 85 ± 6% (*sas-6-sg*; Mean ± SD; N = 78–372; Fig 2D), which are consistent with the reported phenotypes of their RNAi animals (Gonczy *et al*, 2000; Sonnichsen *et al*, 2005). Thus, we constructed conditional mutations of embryonically essential centriole genes (*sas-4, sas-5*, and *sas-6*).

We next examined the ciliary morphology in these conditional mutant animals. Using an OSM-6/IFT52::GFP reporter that marks an IFT-particle subunit moving along the entire cilium, we found that the GFP fluorescence of OSM-6::GFP was visible in the dendrite but was absent in 14 ± 7%, 23 ± 7%, and 18 ± 1% of *sas-4-sg, sas-5-sg,* and *sas-6-sg* animals, respectively (Mean ± SD; N = 28–76; the representative images are shown in Figs 2E and EV1D), indicating the lack of IFT in the absence of the centriolar proteins in amphid and phasmid cilia. The similar lack of OSM-6::GFP fluorescence was also observed in cilia of the PQR neuron, with the penetrance of 15 ± 2%, 33 ± 11% and 30 ± 14% of *sas-4-sg, sas-5-sg*, and *sas-6-sg* (Mean ± SD; N = 12–20; the representative images are shown in Fig 2E). We further examined the transition zones in these mutant animals. The transition zone is a subdomain of the cilium characterized by Y-shaped fibers connecting the doublet microtubules and ciliary membrane and functioning as a ciliary gate to regulate IFT (Williams *et al*, 2011). We generated a mMaple3 knock-in animal of MKS-5 (Meckel-Gruber syndrome) protein to visualize the transition zone and mMaple3-tagged MKS-5 localized at the ciliary base in 100% of the WT adult animals. In consistent with the absence of OSM-6::GFP in cilia, no fluorescence of MKS-5::mMaple3 could be detected at the base of cilia, with the penetrance of 12 ± 3%, 27 ± 10%, and 15 ± 1% in amphid and phasmid cilia of the adult *sas-4-sg, sas-5-sg*, or *sas-6-sg* animals, respectively (Mean ± SD; N = 46–106; the representative images are shown in Fig 2F). The TZ defects were also detected in PQR neuron as 18 ± 2%, 40 ± 1%, and 17 ± 4% of *sas-4-sg, sas-5-sg*, or *sas-6-sg* animals were lack of MKS-5::mMaple3 fluorescence intensity around their transition zones (Mean ± SD; N = 17–67; the representative images are shown in Fig 2F). We next examined the MKS-5 accumulation in L1 larvae in the absence of the core centriole proteins. Our live imaging analysis showed that the MKS-5::mMaple3 fluorescence was enriched as puncta in the dendrite 68 ± 23 min after the dendrite elongates in WT animals (Fig 5A; N = 54). By contrast, MKS-5::mMaple3 did not form any puncta in 29% of *sas-5-sg* conditional mutants after the time-lapse recording for 2–3 h (Mean ± S.D.; N = 49; the representative images and movie are shown in Fig 2G and I, and in Movie EV2). Although 24% of the *sas-5-sg* animals eventually formed the MKS-5 fluorescence puncta at the dendrite tip, the process was severely retarded, taking 125 ± 33 min (Mean ± SD; N = 49; the representative images and movies are shown in Fig 2H and I, and in Movie EV2). The delayed formation of MKS-5 puncta in 24% of *sas-5-sg* conditional mutants is likely because residual SAS-5 builds a deformed centriole that is not as good at templating the cilium. Conditional mutations of *sas-5* may not completely remove SAS-5 as it is essential for cell division and other events before ciliogenesis, and the absence of GFP::SAS-5 fluorescence in *sas-5-sg* animals may not indicate the complete loss of SAS-5, making it difficult to examine the role of residual SAS-5 in partial ciliogenesis. We cannot exclude the possibility that cells may form cilia without centrioles but not very efficiently. Together, these data indicate that centriolar proteins are essential for ciliogenesis in *C. elegans*.

Centriole translocation depends on the cytoplasmic dynein-1

We next investigated the mechanism underlying centriole translocation along the dendrite. To explore microtubule polarity in the developing dendrites of L1 larvae, we constructed the microtubule plus-end binding protein EBP-2::GFP knock-in strain. The fluorescence of EBP-2::GFP appeared as comet-like streaks in the *C. elegans* embryos and in adult somatic cells (Movie EV3). As shown in the kymograph in Fig 3A, 80% of the EBP-2::GFP comets moved away from the growth cone to the cell body at 0.22 ± 0.11 μm/s, whereas the other 20% of the EBP-2::GFP comets moved in the opposite direction with a speed of 0.22 ± 0.11 μm/s, indicating that dendritic microtubules mostly emanate from the tip of the dendrite (Mean ± SD; N = 223 tracks in 12 cells; the representative images are shown in Figs 3A and EV3A). Consistently, in sensory neurons of adult *C. elegans*, 94% of EBP-2::GFP moved from the cilium base toward the cell body (Hao *et al*, 2011). The

Figure 2. Centriolar proteins are essential for ciliogenesis in *Caenorhabditis elegans* neurons.

A Schematic representation of the cartwheel viewed from the proximal end. The nine symmetric cartwheel central hub is composed of SAS-6 (blue), where SAS-5 (red) localizes at the interior of centriole, and appears to function as a linker between SAS-6 and SAS-4 (green). SAS-4 localizes more toward the periphery of the centriole, which associates with microtubules.

B Gene models of centriolar proteins for generating conditional mutations; exons are shown as boxes, and arrows indicate sgRNA sequences corresponding to exons (Table EV1).

C Representative gels showing the T7EI assay results for *sas-4-sg, sas-5-sg,* and *sas-6-sg*. PCR products amplified from the genomic DNA of worms expressing P*hsp::Cas9* and P*U6::sas-4,5,6-sg* after heat-shock treatment. Indels are indicated at the bottom.

D Embryonic lethality was determined by quantifying viable embryos after heat-shock treatment. N = 78–372; Mean ± S.D. (error bars). ****P < 0.0001 based on Student's t-test. N.S., not significant.

E Ciliary morphology (amphid, phasmid, and PQR neuron) in conditional mutants as visualized by OSM-6::GFP. The penetrance was quantified at 0 ± 0% for WT (N = 62), 14 ± 7% for *sas-4-sg* (N = 76, P < 0.05), 23 ± 7% for *sas-5-sg* (N = 65, P < 0.01), and 18 ± 1% for *sas-6-sg* (N = 28, P < 0.001). Yellow asterisks indicate the location of ciliary base. Blue arrows mark the distribution of IFT particles along cilia.

F Transition zone morphology in conditional mutants visualized by MKS-5::mMaple3. The penetrance is 0 ± 0%, 12 ± 3%, 27 ± 10%, and 15 ± 1% for WT (N = 46), *sas-4-sg* (N = 69, P < 0.05), *sas-5-sg* (N = 98, P < 0.01), and *sas-6-sg* (N = 106, P < 0.001), respectively. Yellow asterisks indicate the location of ciliary base.

G–I (G, H) Fluorescence time-lapse images of MKS-5::mMaple3 accumulation in *sas-5* mutant animals. Quantification is shown in (I), no accumulation (> 150 min), delayed accumulation (120–150 min), and normal (< 120 min) (N = 49) (Movie EV2).

Data information: Scale bars, 5 μm.

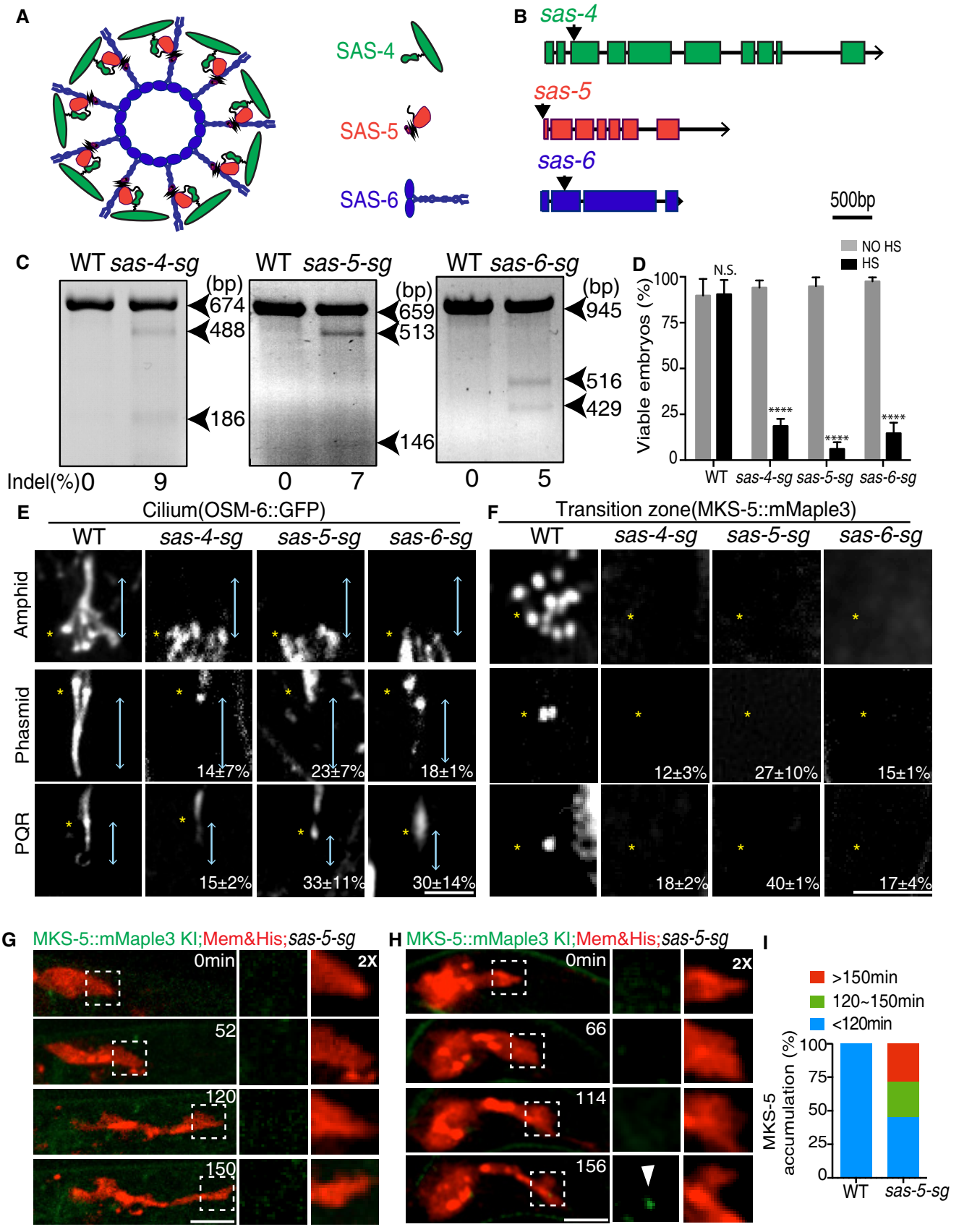

Figure 2.

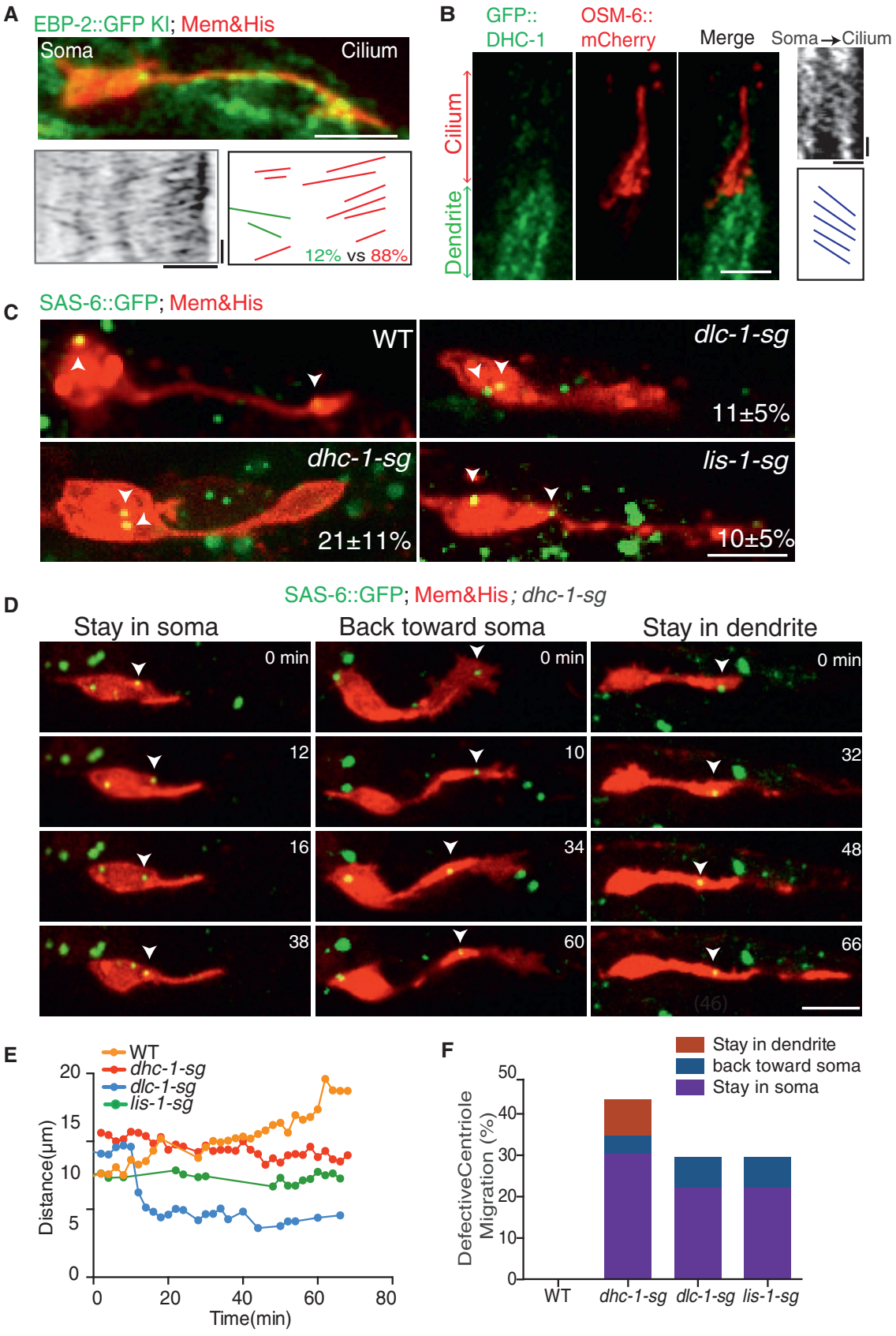

Figure 3.

Figure 3. Centriole translocation requires cytoplasmic dynein-1.

A EBP-2::GFP protein dynamics in PQR neuron during ciliogenesis in L1 larva (top). A kymograph (left bottom) with corresponding cartoons (right bottom) showing 80% of EBP-2::GFP comets move from cilium to soma at the speed of 0.22 ± 0.11 μm/s (N = 223) (Movie EV3).

B Dynein motility in dendrites of ciliated neurons. A kymograph (right top) with corresponding cartoons (right bottom) showing the soma-to-cilium directed movement of dynein; scale bars, 2 μm, 10 s.

C Centriole movement defects in conditional mutants visualized by SAS-6::GFP; 21 ± 11% for *dhc-1-sg* (N = 152, $P < 0.01$), 11 ± 5% for *dlc-1-sg* (N = 92, $P < 0.01$), and 10 ± 5% for *lis-1-sg* (N = 76, $P < 0.05$).

D–F (D, F) Fluorescence time-lapse images and quantification of centriole positioning during ciliogenesis in Dynein-1 mutants. Among these cells, 30% show two immobile centrioles remaining in the soma (left), 9% have one centriole in the dendrite without continuous movement toward the dendrite tip (middle), and 4% contain centriole that underwent backward migration to the cell body (right) (N = 46). Note that at 0 min dendrite already extended more than 1 μm (Movie EV4). (E) The centriole displacement tracks in Dynein-1 mutants compared with wild-type animals; the quantification is shown in (F).

Data information: Scale bars, 5 μm except for Fig 3B.

orientation of microtubules and the unidirectional movement of centrioles along the dendrite suggest that a minus-end-directed microtubule motor protein might be involved. Importantly, by visualizing DHC-1 localization in a GFP::DHC-1 animal, we showed that DHC-1 was restricted within the dendrite and did not enter cilia (Fig 3B). We postulate that centriole translocation may be driven by dynein-1 along the dendritic microtubules.

To study the function of dynein-1 in centriole translocation, we examined the position of centrioles of PQR neuron in the *dhc-1-sg* conditional mutant strain. At the late L1 larval stage, centriole translocation was completed in the dendrite of WT PQR neurons. However, in 21 ± 11% of *dhc-1-sg* mutant animals (N = 152) that properly elongated their dendrites, no centrioles could be detected in the dendrite; instead, two centrioles were retained in the cell body. Conditional mutations of the dynein-1 light-chain LC8 or the associated subunit Lissencephaly protein LIS-1 caused the same defects of centriole translocation, with penetrance of 11 ± 5% for *dlc-1-sg* (N = 92) and 10 ± 5% for *lis-1-sg* (N = 76; Fig 3C). To address which aspects of centriole movement require dynein-1, we followed centriole behavior in dynein-1 conditional mutant animals. For these live cell imaging analyses, our time-lapse recording started when the dendrite was over 1.5 μm in length. Three patterns of centriole behavior indicated the effects of dynein-1 inhibition. In one pattern, 30% of cells retained two immobile centrioles in the soma, while the dendrite extended; in the second pattern, 9% of cells had one centriole in the elongating dendrite but this centriole did not show any continuous movement toward the dendrite tip; in the third pattern, centriole neared the dendrite tip in 4% of cells but underwent backward movement to the soma (Fig 3D–F; N = 46). These phenotypes were reproducibly observed in *dlc-1-sg* (22% for staying in soma; 7% for backward movement; N = 27) and in *lis-1-sg* conditional mutant animals (9% for non-motile in the dendrite; 9% for backward movement; N = 11; the representative images and movie are shown in Figs 3E and F, and EV3B and C; Movie EV4). The conditional mutations of *dlc-1* or *lis-1* reduced ciliary length and disrupted the ability of these cilia to uptake fluorescence dye (i.e., the Dyf phenotype; Li *et al*, 2015). Consistently, we found that the lack of DHC-1 caused Dyf phenotype in 23 ± 5% animals (N = 165 from three generations, Mean ± SEM). Importantly, the cilium length was significantly reduced from ~8 μm in WT animals to 3.7 ± 0.4 μm in *dhc-1* conditional mutant worms (N = 48, Mean ± SEM; the representative images are shown in Fig EV3D and E). Overall, our results indicate that the cytoplasmic dynein-1 is required for centriole translocation along the growing dendrite.

LC8 and SAS-5 bind *in vitro* and colocalize *in vivo*

We next sought to understand how dynein-1 is involved in the translocation of centriolar proteins. The recent structural study provided evidence that dynein light-chain LC8 dimers bind to the *Drosophila* Ana2/SAS-5 (Slevin *et al*, 2014). Using an anti-GFP antibody, we purified GFP-tagged SAS-5 with its associated proteins from the lysate of transgenic *C. elegans* larvae that expressed GFP::SAS-5 (Fig 4B). Protein constituents were determined by means of liquid chromatography–tandem mass spectrometry. Two interesting hits from the purification were the dynein light-chain DLC-1/LC8 and heavy-chain DHC-1 from the dynein-1 complex (Fig 4A and B; Datasets EV1 and EV2). To examine the interactions between DLC-1 and SAS-5, we performed a GST pulldown assay using the purified GST-DLC-1 and the worm lysate containing GFP::SAS-5. As shown in Fig 4C, GFP::SAS-5 was detected to associate with GST-DLC-1 but not GST control. We further demonstrated a direct interaction between DLC-1 and SAS-5 using the pulldown assay with the purified GST-DLC-1 and His-GFP-SAS-5 (Fig 4D). Moreover, our GFP-affinity purification of binding partners of SAS-6 also identified components of the dynein-1 motor complex (Fig EV4A and B; Datasets EV1 and EV2).

Given the above genetic and biochemical observations, we examined where DLC-1 might regulate centriole translocation. To this end, we constructed a DLC-1::GFP knock-in strain to visualize the localization of the dynein light-chain LC8 during Q neuroblast development. Live imaging analysis showed that the DLC-1::GFP fluorescence was enriched as puncta at the spindle pole where centrioles localize during Q cell division. After Q cell division and migration, one of the two GFP puncta entered the growing dendrite and underwent the directional movement toward the dendritic tip as the motile centriole at the velocity of 0.11 ± 0.03 μm/min (Figs 4E and EV4C; Movie EV3). Our data suggest that the dynein-1 powers centriole translocation likely via the direct interaction between LC8 and SAS-5.

The sequential recruitment of transition zone and IFT proteins

We next examined the sequence of the recruitment of transition zone proteins and IFT components in relation to the loss of centriolar proteins. Using an MKS-5::mMaple3 knock-in strain, we showed that the green fluorescence of MKS-5::mMaple3 signal was first detected at 68 ± 23 min after the dendrite started to grow (Fig 5A and C; Movie EV2; Mean ± SD, N = 54). A second-order polynomial (quadratic) model appeared to fit the increase in fluorescence over time from the MKS-5::mMaple3 spot (Figs 5D and EV5A). For the IFT components, the OSM-6::GFP fluorescence emerged

A

IP (% Sequence Coverage)

Copurified Protein	GFP::SAS-5
SAS-5	82.92
SAS-6	13.41
DLC-1	25.84
DHC-1	1.01

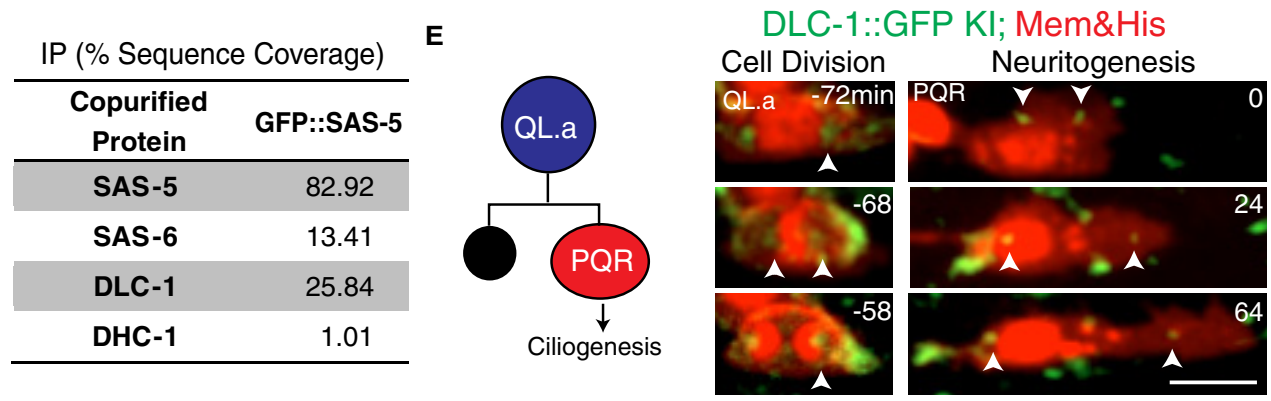

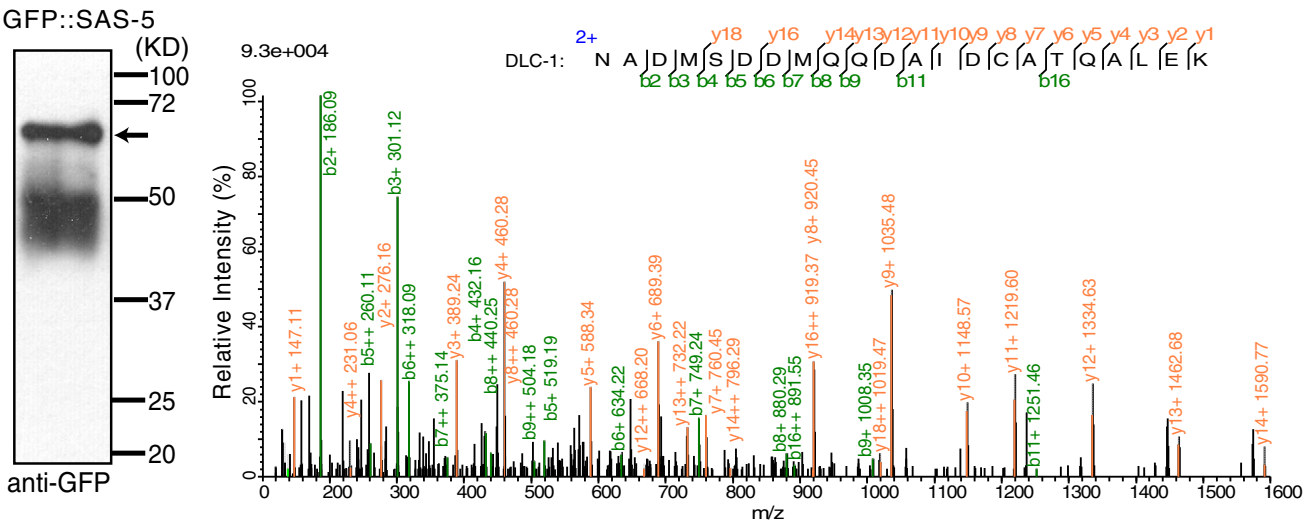

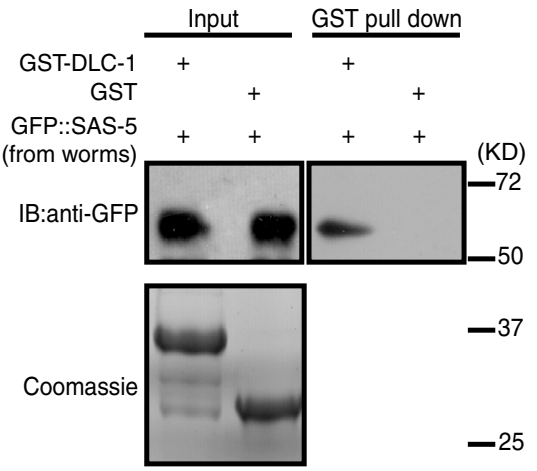

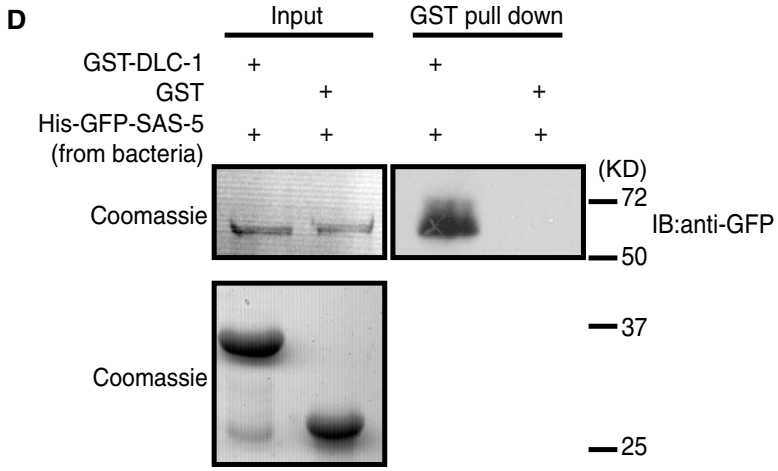

Figure 4. Dynein light-chain LC8/DLC-1 interacts with SAS-5 *in vitro* and colocalizes *in vivo*.

A Mass spectrometry analysis of the indicated affinity purifications. The percentage of sequence coverage was listed.

B Western blot with anti-GFP antibody showing the immunoprecipitation of GFP::SAS-5 from *C. elegans* using GFP-TrapA beads (left). The mass spectrum of a unique peptide NADMSDDMQQDAIDCATQALEK in DLC-1 (LC8).

C SAS-5 interacts with DLC-1. GST pulldown assay using GST-DLC-1 and worm lysate from the strain expressing GFP::SAS-5.

D Direct interaction between SAS-5 and DLC-1 by GST pulldown assay using GST-DLC-1 and His-GFP-SAS-5.

E Schematic representation showing asymmetric cell division to generate PQR and neuritogenesis of PQR to form the cilium (left). Fluorescence time-lapse images of GFP-tagged DLC-1 localization during cell division and neuritogenesis (right) (Movie EV3). Scale bar, 5 μm.

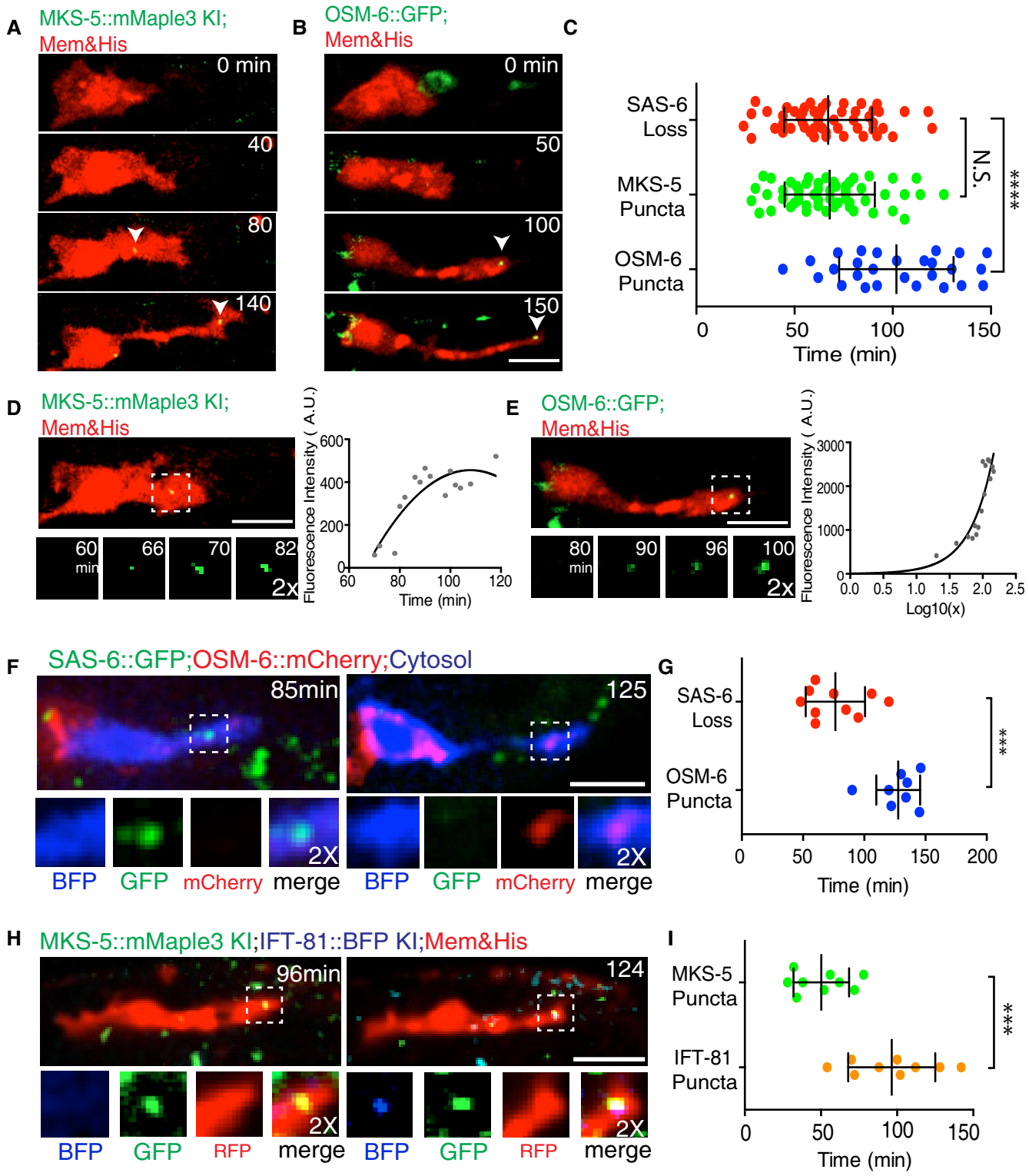

Figure 5.

approximately 102 ± 29 min after the initiation of dendritic growth (Fig 5B and C; Movie EV2; Mean ± SD, $N = 27$), and an exponential growth equation model was applied to fit the increase in the fluorescence of OSM-6::GFP over time (Figs 5E and EV5B). These observations reveal the different timings and patterns of protein enrichment in the formation of the transition zone and cilium. Our comparison of the time points of centriolar protein elimination and transition zone protein accumulation did not reveal any significant differences ($P = 0.85$, t-test), suggesting that centriolar proteins were removed when the transition zone started to form. By contrast,

Figure 5. The sequential recruitment of transition zone and IFT proteins.

A MKS-5 accumulation during ciliogenesis. Arrow indicates the MKS-5 punctum (Movie EV2).

B The OSM-6 accumulation. Arrow indicates OSM-6 punctum (Movie EV2).

C Quantification and comparison of the time for SAS-6 loss, MKS-5 accumulation, and OSM-6 accumulation. SAS-6 disappears at 65 ± 22 min after time 0 (N = 53). The MKS-5 puncta appear at 68 ± 23 min (N = 54, N.S. vs. SAS-6 loss), and OSM-6 accumulates at 102 ± 29 min (N = 27, ****P < 0.0001 vs. SAS-6 loss). N.S., not significant.

D A representative fluorescence accumulation of MKS-5 (left) and a trace of the fluorescence increase fitted with a second-order polynomial (quadratic) model (right). More traces are in Fig EV5A.

E A representative fluorescence accumulation of OSM-6 (left) and a trace of the fluorescence increase fitted with an exponential growth model (right). More traces are in Fig EV5B.

F Time-lapse images of centriole degeneration (SAS-6::GFP), IFT accumulation (OSM-6::mCherry), and the PQR cytosol (P*lin-32*::TagBFP) (Movie EV5).

G Quantification of the time sequences: 76 ± 23 min for SAS-6 loss and 128 ± 17 min for OSM-6 accumulation (N = 8, ***P < 0.001).

H Time-lapse images of transition zone formation (MKS-5::mMaple3), IFT accumulation (IFT-81::BFP), and the PQR membrane (P*egl-17::myri*::TagRFP) (Movie EV5).

I Quantification of the time sequences: 63 ± 24 min for MKS-5 accumulation and 95 ± 28 min for IFT-81 accumulation (N = 8, ***P < 0.001).

Data information: Mean ± SD; Student's t-test; Scale bars, 5 μm.

IFT-protein accumulation was significantly later than either centriolar protein elimination or the transition zone formation (P < 0.0001; Figs 5C and EV5C).

We conducted triple-fluorescence live imaging analysis to further confirm the above sequences. For these experiments, we generated the fluorescent animals expressing SAS-6::GFP OSM-6::mCherry, and TagBFP-labeled cytosol of PQR. The fluorescence of SAS-6::GFP disappeared at 76 ± 23 min after the dendritic growth, and OSM-6::mCherry fluorescence was not enriched at the dendrite tip until 49 ± 12 min after the loss of SAS-6::GFP (Fig 5F and G; Movie EV5; Mean ± SD; N = 8, P < 0.001). In an animal expressing MKS-5::mMaple3 KI, IFT-81::TagBFP KI and mCherry-labeled PQR plasma membrane and histone, MKS-5 in the transition zone (63 ± 24 min) was enriched 32 ± 11 min earlier than the accumulation of IFT-81 protein (95 ± 28 min; Fig 5H and I; Movie EV5; Mean ± SD; N = 8). Together, our data show that centriolar proteins are lost at around the same time as the formation of the transition zone but earlier than the enrichment of IFT components at the dendrite tip.

Discussion

In summary, this study has defined the subcellular events during neuronal ciliogenesis in a developing sensory neuron in *C. elegans*. We provide evidence that dynein-dependent centriole translocation, elimination of centriole subunits, and the sequential recruitments of transition zone and IFT components are involved in this process. We suggest that the formation of olfactory cilia in mammalian OSNs may use mechanisms similar to those delineated here.

How a centriole imparts the ninefold symmetry information to template axonemal microtubules during ciliogenesis has been a long-standing question in developmental neurobiology. Axonemal microtubules are invariably organized in a radial ninefold symmetry, which is thought to originate from the nine spokes in the cartwheel. Centriole satellites are essential for ciliogenesis (Anderson, 1972; Vorobjev & Chentsov Yu, 1982; Tanos *et al*, 2013; Tateishi *et al*, 2013); the *C. elegans* homolog of hydrolethalus syndrome protein 1 (HYLS-1) is required for anchoring of centrioles at the plasma membrane in sensory neurons (Dammermann *et al*, 2009; Wei *et al*, 2016). HYLS-1 marks the centriolar MTs that spread out at the base of worm cilia, presumably due to the loss of the central tube (Dammermann *et al*, 2009; Doroquez *et al*, 2014). Consistent with this notion, we show that HYLS-1 localizes at the centriole and persists at the base of the mature cilia (Fig EV5D). The central tube may become unnecessary for the subsequent formation of the transition zone or recruitment of ciliary components, which may explain the elimination of the centriole tube before the recruitment of IFT subunits.

Why does the centriole degenerate during ciliogenesis? Previous TEM results have shown that centriole degeneration appears to occur shortly after the onset of ciliogenesis during late embryogenesis (White *et al*, 1986; Nechipurenko *et al*, 2017; Serwas & Su, 2017), which is consistent with the loss of GFP fluorescence of SAS-6 around transition zone formation (Fig 1B). During the mammalian cell cycle, SAS-6 protein is degraded at the end of mitosis and accumulates again beginning in the late G1 phase, and the ectopic higher levels of SAS-6 promote the formation of excess procentrioles or centrioles (Strnad *et al*, 2007; Arquint *et al*, 2012). The elimination of centriolar proteins may prevent the formation of excess centrioles, ensuring the correct cilium number in a given cell. Although the basal bodies retain at the base of the cilium in mammalian OSNs (Falk *et al*, 2015), it remains to be examined whether cartwheel proteins such as SAS-6 is localized in these basal bodies, leaving it an open question whether the mammalian centriolar proteins are removed, like their *C. elegans* homologs, during olfactory ciliogenesis.

How are centriolar proteins lost in the developing dendrite? In a mitotic cell, APC^{Cdh1} targets SAS-6 to the 26S proteasome for degradation (Arquint *et al*, 2012). Recent studies have uncovered the functional interactions between autophagy and ciliogenesis: Removal of OFD1 by autophagy at centriolar satellites promotes ciliogenesis, whereas the degradation of IFT proteins by autophagy regulates ciliary length (Tang *et al*, 2013). Centriole degeneration during ciliogenesis may also require the contribution of the 26S proteasome or autophagy. However, the SAS-6::GFP fluorescence persists throughout the cell cycle in the Q neuroblast lineages (Figs 1B and EV1B), suggesting that centriole degeneration in *C. elegans* may utilize additional mechanisms. The motile centriole in the dendrite degenerates, whereas the non-motile centriole in the cell body remains, suggesting that the degradation activity is tightly controlled based on the subcellular location or that two centrioles show distinct responses to degeneration signal. In support of the distinct fates of these two centrioles, the immotile centriole also has centriolar proteins that interact with dynein-1 and DLC-1; however, its motility could be barely detected during PQR development (Figs 1C and D, and 4E).

This work uncovers an important role of cytoplasmic dynein-1 in centriole translocation along the dendrite. We identify a direct

interaction between the dynein light-chain LC8 and SAS-5 and suggest that this interaction may couple dynein-1 with the centriole. This interaction pair was previously reported from the *Drosophila* neuroblast asymmetric division (Wang *et al*, 2011). Crystallographic studies showed that four LC8 dimers bind to the central region of the *Drosophila* Ana2/SAS-5 and that these LC8-binding sites are not readily apparent in the *C. elegans* SAS-5 (Slevin *et al*, 2014). Our biochemical data revealed that the interaction between DLC-1 and SAS-5 is conserved in *C. elegans*. It remains unclear how LC8 bridges the dynein motor complex to the centriolar protein complex; further, some species possess LC8 but do not have the dynein heavy chain, suggesting that LC8 can localize with the centriole hub in a complex with SAS-5, independent of the dynein motor (King, 2008; Lightcap *et al*, 2008). However, our mass spectrometric analysis of the binding partners of GFP::SAS-5 detected both LC8 and the dynein motor; importantly, conditional mutations of the dynein motor and LC8 caused the same defects on centriole translocation, indicating that the dynein-1 motor and LC8 function together to transport the centriole. Cytoplasmic dynein-1 is the only microtubule minus-end motor that we examined in this study, and we cannot exclude the possibility that other minus-end kinesin motors are involved in centriole translocation. The speed of centriole translocation along the dendrite is 0.08 ± 0.01 μm/min ($N = 31$); intriguingly, the centriole was moved by dynein-1 at a relatively constant rate of 0.1 μm/min in migrating neural precursors of the mouse brain tissue (Tsai *et al*, 2007). Despite the similar translocation speeds of the *C. elegans* centriole and the mammalian centrosome, the cytoplasmic dynein-1 can move at > 1 μm/s in live cells (Pilling *et al*, 2006; Reck-Peterson *et al*, 2006; Moughamian & Holzbaur, 2012; Maday *et al*, 2014). As shown in the kymograph of GFP::DHC-1 along the dendrite, dynein-1 moves at 0.18 ± 0.09 μm/s in *C. elegans* neurons (Mean ± SD; $N = 73$; the representative images are shown in Fig 3B). The speed discrepancy may result from the transient interaction between centriole and dynein or multiple mechanisms may be involved at different stage of centriole translocation.

Transmission electron microscopy studies revealed two general phases of ciliogenesis. The early phase includes the binding of ciliary vesicles to the basal body, after which the transition zone emerges and matures through fusion of secondary vesicles until the ciliary gate is formed. The late phase includes axoneme extension in which ciliary precursors are delivered into the growing cilia by IFT-protein machinery (Sorokin, 1962; Reiter *et al*, 2012). In addition to the shared steps, different sensory neurons can apply distinct mechanisms to position their centrioles. Basal bodies were initially located at the dendrite tips in sensory neurons of *C. elegans* embryos (Dammermann *et al*, 2009; Schouteden *et al*, 2015), whereas the centriole in PQR translocates to the dendrite tip. Future studies may uncover other fascinating mechanisms of ciliogenesis from the mammalian olfactory system that consists of millions of OSNs.

Materials and Methods

Caenorhabditis elegans strains, genetics and DNA manipulations

Caenorhabditis elegans strains were cultivated on NGM plate seeded with the *Escherichia coli* strain OP50 at 20°C according to standard protocols. To generate conditional knockout mutants, CRISPR-Cas9 plasmid construction and injection was carried out as described previously (Li *et al*, 2015). For transgenic expression, DNA plasmids were microinjected to the germline at 10–50 ng/μl with co-injection markers *pRF4* [*rol-6 (su1006)*] and/or *Podr-1::dsRed* into N2 or co-injection the *unc-76*-rescuing plasmid p76-16B into *unc-76 (e911)* animals. To express mMaple3 in *C. elegans*, we reengineered it by changing its codon use and inserting artificial introns according to the original sequences (Green *et al*, 2008; Wang *et al*, 2014). For knock-in repair template, briefly, GFP- or mMaple3-fluorescent protein gene flanked by 1-1.5kb upstream and downstream homologous arms of target gene was inserted into *pPD95.77* via In-Fusion Advantage PCR Cloning Kit (Clontech). Knock-in strains were selected and confirmed by PCR. A complete list of strains, primers, and plasmids can be found in the Tables EV1 and EV2.

Heat-shock treatment and viability

Approximately 100 eggs that were laid after 4–6 h were collected and treated with heat-shock (33°C for 1 h) to generate conditional mutation. For viability assay, eggs survived from heat-shock treatment were grown into young adults; viability is defined as the hatched worms divided by the number of the original eggs. All data were collected from more than three generations.

Molecular assay

The detection of molecular lesions induced by conditional knockout via CRISPR-Cas9 strategy followed previous methods (Shen *et al*, 2014). Genomic DNA was isolated from heat-shock-treated worm lysis, the target fragments were amplified by PCR, and purified DNA was digested by 5 units of T7 endonuclease I (New England Biolabs) at 37°C for 30 min. Indel percentage was determined by the formula $100\times\ (1 - (1 - (b + c)/(a + b + c))^{1/2})$, where a is the integrated intensity of the intact band and b and c are the integrated intensities of digested small bands.

Live cell imaging

Caenorhabditis elegans L1 larvae were anesthetized with 1 mg/ml levamisole in M9 buffer, mounted on 3% agarose pads, and maintained at 22°C (Chai *et al*, 2012). Imaging system includes an Axio Observer Z1 microscope (Carl Zeiss MicroImaging, Inc.) equipped with a 100X, 1.45 N.A. objective, an EM CCD camera (Andor iXon+ DU-897D-C00-#BV-500), and the 488-nm and 568-nm lines of a Sapphire CW CDRH USB Laser System to a spinning disk confocal scan head (Yokogawa CSU-X1 Spinning Disk Unit). Time-lapse images were acquired with exposure time of 200 ms with 3 μm Z stack projection at every 2 min for imaging the entire ciliogenesis process. Images were acquired by μManager (www.micro-manager.org), and images were processed and quantified by ImageJ software (http://rsbweb.nih.gov/ij/).

Quantifications and statistical analysis

To quantify the centriole translocation during PQR ciliogenesis, the PQR is rotated to the anterior–posterior direction, the time zero of PQR ciliogenesis was defined as the completion of cell migration of

the PQR cell. The centriole position is digitalized as the XY coordinate, and the parameters such as distance and time were calculated by the XY coordinate of each time point relative to the soma (Fig EV2A). The formation of transition zone and IFT proteins were determined by the appearance of the fluorescence spot at the dendrite tip, and the time gap between two processes was compared and calculated. Student's *t*-test and chi-square analysis were used to examine statistical differences of ciliary phenotypes between WT and mutants as indicated in the figure legends, and two-sided *P*-value was shown.

Protein purification

We amplified *sas-5* and *dlc-1* cDNA from a *C. elegans* cDNA library. Full-length SAS-5 tagged with GFP and DLC-1 were cloned in pET15a and pGEX4T vectors, respectively. The resultant plasmids were transformed to *E. coli* strain BL21 (DE3) and grown at 37°C in LB media to produce His-GFP-SAS-5 and GST-DLC-1 protein. Protein expression was induced at OD600 0.6 by isopropyl-β-D-1-thiogalactopyranoside (IPTG, 0.3 mM final concentration) at 16°C. After ~16 h, *E. coli* were harvested and disrupted by sonication in the lysis buffer [25 mM Tris-HCl (pH 7.5), 150 mM NaCl, 0.5% Nonidet P40, 10% glycerol] supplemented with protease inhibitor cocktail (cOmplete, Roche, Basel, Switzerland). After centrifugation at 40,000 *g* for 30 min, cell lysate of His-GFP-SAS-5 was incubated with nickel beads for 60 min at 4°C. Resin beads were washed with lysis buffer supplemented with 20 mM imidazole, and protein was eluted with lysis buffer supplemented with 500 mM imidazole followed by gel filtration using the chromatography system (BioLogic DuoFlow; Bio-Rad Laboratories) with a Superdex 200 10/300 GL column (GE Healthcare; equilibrated with lysis buffer containing 1 mM DTT). Cell lysate of GST-DLC-1 was incubated with glutathione Sepharose beads for 60 min at 4°C. Beads were washed with PBS containing 250 mM NaCl and re-equilibrated in PBS supplemented with 20% glycerol and were flash-frozen in liquid nitrogen for pulldown assay.

Pulldown assay

2 ml of worm pellet expressing GFP::SAS-5 was mixed with 2 ml lysis buffer containing protease inhibitors and 4 ml of 0.5-mm-diameter glass beads, and was disrupted with FastPrep-24 (MP Biomedicals) at 6.5 m/s, 15 s/pulse × 5 pulses with 5-min intervals on ice. Lysates were clarified by centrifugation at 12,000 *g* for 30 min and were mixed with the beads associated with 30 μg GST-DLC-1 or GST for 60 min at 4°C. The beads were washed with lysis buffer supplemented with 250 mM NaCl and resuspended with a SDS sample buffer followed by SDS-PAGE. For pulldown assays using the purified proteins, 10 μg His-GFP-SAS-5 was incubated with beads associated with 30 μg GST-DLC-1 or GST protein. The reaction was performed in 50 μl lysis buffer for 60 min at 4°C, and the beads were washed and resuspended in a SDS sample buffer followed by Western blot analysis with anti-GFP antibody (Roche, # 11814460001,RRID:AB_390913).

Mass spectrometry analysis

GFP::SAS-5 and SAS-6::GFP mass spectrometry was performed as previously described (Falkner & Andrews, 2005). Worms were lysed and clarified with same protocol in pulldown assay. Cleared worm extracts were incubated with the GFP-Trap A beads (Chromoteck) for 60 min and washed three times with lysis buffer. Immunoprecipitates were dissolved from the GFP-IP beads in 100 mM Tris, pH 8.5 and 8 mol/l urea. Proteins were reduced with 5 mM TCEP and alkylated with 10 mM Iodoacetamide followed by digestion with trypsin at 37°C for 14 h. The resulting peptides were analyzed twice on a Q Exactive mass spectrometer (ThermoFisher Scientific) interfaced with an Easy-nLC1000 liquid chromatography system (ThermoFisher Scientific). Peptides were loaded on a 75 μm × 4 cm trap column packed with 10 μm, 120 Å ODS-AQ C18 resin (YMC Co., Ltd. Kyoto, Japan) and connected to a 75 μm × 10 cm analytical column packed with 1.8 μm, 100 Å Luna C18 resin (Welch Materials, Shanghai, China). After desalting, peptides were separated at a flow rate of 200 nl/min with a 79-min linear gradient from 5% buffer B (100% ACN, 0.1% FA), 95% buffer A (0.1% FA) to 28% buffer B followed by a 10-min gradient to 80% buffer B, 3-min gradient to 100% buffer B and maintaining at 100% buffer B for 10 min. The top 15 most abundant precursor ions from the survey scan were selected for higher-energy collisional dissociation (HCD); R = 70,000 in full scan, R = 17,500 in HCD scan; AGC targets were 3e6 for FTMS full scan, 1e5 for MS2; minimal signal threshold for MS2 = 5e4; +1 and unassigned precursors are excluded; normalized collision energy is 27 for HCD; dynamic exclusion is 30 s; ion 445.12003 is used for internal calibration. Raw data were extracted using the RawXtract software. The MS/MS spectra were searched against the *C. elegans* protein database using with Prolucid (Xu *et al*, 2015) and the search results of the two technical replicates were filtered separately using DTASelect 2 (Tabb *et al*, 2002) by requiring 1% FDR at the peptide level, precursor mass accuracy ≤5 ppm, Z score ≥ 4, and a minimum of one peptide for a protein ID. The FDR rates at the protein level were 0.61 and 1.76%, respectively. The complete MS dataset is provided in Datasets EV1 and EV2.

Expanded View for this article is available online.

Acknowledgements
We thank the Protein Chemistry Facility at the Center for Biomedical Analysis of Tsinghua University for sample analysis. This study was supported by the National Basic Research Program of China (2017YFA0503501, 2017YFA0102900 and 2013CB945602) and the National Natural Science Foundation of China (31190063 and 31301134).

Author contributions
GO and WJL conceived the experiments; WJL, PY, ZZ, XZ, and WL performed the experiments; and GO and WJL wrote the manuscript.

Conflict of interest
The authors declare that they have no conflict of interest.

References

Anderson RG (1972) The three-dimensional structure of the basal body from the rhesus monkey oviduct. *J Cell Biol* 54: 246 – 265

Arquint C, Sonnen KF, Stierhof YD, Nigg EA (2012) Cell-cycle-regulated expression of STIL controls centriole number in human cells. *J Cell Sci* 125: 1342 – 1352

Berbari NF, Johnson AD, Lewis JS, Askwith CC, Mykytyn K (2008) Identification of ciliary localization sequences within the third intracellular loop of G protein-coupled receptors. *Mol Biol Cell* 19: 1540 – 1547

Brown JM, Witman GB (2014) Cilia and diseases. *Bioscience* 64: 1126 – 1137

Cabral G, Sans SS, Cowan CR, Dammermann A (2013) Multiple mechanisms contribute to centriole separation in *C. elegans*. *Curr Biol* 23: 1380 – 1387

Chai Y, Li W, Feng G, Yang Y, Wang X, Ou G (2012) Live imaging of cellular dynamics during *Caenorhabditis elegans* postembryonic development. *Nat Protoc* 7: 2090 – 2102

Challis RC, Tian H, Wang J, He J, Jiang J, Chen X, Yin W, Connelly T, Ma L, Yu CR, Pluznick JL, Storm DR, Huang L, Zhao K, Ma M (2015) An olfactory cilia pattern in the mammalian nose ensures high sensitivity to odors. *Curr Biol* 25: 2503 – 2512

Cuschieri A, Bannister LH (1975a) The development of the olfactory mucosa in the mouse: electron microscopy. *J Anat* 119: 471 – 498

Cuschieri A, Bannister LH (1975b) The development of the olfactory mucosa in the mouse: light microscopy. *J Anat* 119: 277 – 286

Dammermann A, Pemble H, Mitchell BJ, McLeod I, Yates JR III, Kintner C, Desai AB, Oegema K (2009) The hydrolethalus syndrome protein HYLS-1 links core centriole structure to cilia formation. *Genes Dev* 23: 2046 – 2059

Delattre M, Leidel S, Wani K, Baumer K, Bamat J, Schnabel H, Feichtinger R, Schnabel R, Gonczy P (2004) Centriolar SAS-5 is required for centrosome duplication in *C. elegans*. *Nat Cell Biol* 6: 656 – 664

Dirksen ER (1974) Ciliogenesis in the mouse oviduct. A scanning electron microscope study. *J Cell Biol* 62: 899 – 904

Doroquez DB, Berciu C, Anderson JR, Sengupta P, Nicastro D (2014) A high-resolution morphological and ultrastructural map of anterior sensory cilia and glia in *Caenorhabditis elegans*. *eLife* 3: e01948

Falk N, Losl M, Schroder N, Giessl A (2015) Specialized cilia in mammalian sensory systems. *Cells* 4: 500 – 519

Falkner J, Andrews P (2005) Fast tandem mass spectra-based protein identification regardless of the number of spectra or potential modifications examined. *Bioinformatics (Oxford, England).* 21: 2177 – 2184

Gonczy P, Echeverri C, Oegema K, Coulson A, Jones SJ, Copley RR, Duperon J, Oegema J, Brehm M, Cassin E, Hannak E, Kirkham M, Pichler S, Flohrs K, Goessen A, Leidel S, Alleaume AM, Martin C, Ozlu N, Bork P *et al* (2000) Functional genomic analysis of cell division in *C. elegans* using RNAi of genes on chromosome III. *Nature* 408: 331 – 336

Green RA, Audhya A, Pozniakovsky A, Dammermann A, Pemble H, Monen J, Portier N, Hyman A, Desai A, Oegema K (2008) Expression and imaging of fluorescent proteins in the *C. elegans* gonad and early embryo. *Methods Cell Biol* 85: 179 – 218

Hagiwara H, Ohwada N, Takata K (2004) Cell biology of normal and abnormal ciliogenesis in the ciliated epithelium. *Int Rev Cytol* 234: 101 – 141

Hao L, Thein M, Brust-Mascher I, Civelekoglu-Scholey G, Lu Y, Acar S, Prevo B, Shaham S, Scholey JM (2011) Intraflagellar transport delivers tubulin isotypes to sensory cilium middle and distal segments. *Nat Cell Biol* 13: 790 – 798

Heiman MG, Shaham S (2009) DEX-1 and DYF-7 establish sensory dendrite length by anchoring dendritic tips during cell migration. *Cell* 137: 344 – 355

Inglis PN, Ou G, Leroux MR, Scholey JM (2007) The sensory cilia of *Caenorhabditis elegans*. In *WormBook*, The *C. elegans* Research Community (ed), doi:10.1895/wormbook.1.126.2

Jenkins PM, McEwen DP, Martens JR (2009) Olfactory cilia: linking sensory cilia function and human disease. *Chem Senses* 34: 451 – 464

King SM (2008) Dynein-independent functions of DYNLL1/LC8: redox state sensing and transcriptional control. *Sci Signal* 1: pe51

Klysik M (2008) Ciliary syndromes and treatment. *Pathol Res Pract* 204: 77 – 88

Leidel S, Gonczy P (2003) SAS-4 is essential for centrosome duplication in *C. elegans* and is recruited to daughter centrioles once per cell cycle. *Dev Cell* 4: 431 – 439

Leidel S, Delattre M, Cerutti L, Baumer K, Gonczy P (2005) SAS-6 defines a protein family required for centrosome duplication in *C. elegans* and in human cells. *Nat Cell Biol* 7: 115 – 125

Li W, Yi P, Ou G (2015) Somatic CRISPR-Cas9-induced mutations reveal roles of embryonically essential dynein chains in *Caenorhabditis elegans* cilia. *J Cell Biol* 208: 683 – 692

Lightcap CM, Sun S, Lear JD, Rodeck U, Polenova T, Williams JC (2008) Biochemical and structural characterization of the Pak1-LC8 interaction. *The Journal of biological chemistry.* 283: 27314 – 27324

Maday S, Twelvetrees AE, Moughamian AJ, Holzbaur EL (2014) Axonal transport: cargo-specific mechanisms of motility and regulation. *Neuron* 84: 292 – 309

Mashukova A, Spehr M, Hatt H, Neuhaus EM (2006) Beta-arrestin2-mediated internalization of mammalian odorant receptors. *J Neurosci* 26: 9902 – 9912

McEwen DP, Jenkins PM, Martens JR (2008) Olfactory cilia: our direct neuronal connection to the external world. *Curr Top Dev Biol* 85: 333 – 370

Menco BP (1980) Qualitative and quantitative freeze-fracture studies on olfactory and nasal respiratory structures of frog, ox, rat, and dog. I. A general survey. *Cell Tissue Res* 207: 183 – 209

Menco BP (1997) Ultrastructural aspects of olfactory signaling. *Chem Senses* 22: 295 – 311

Moughamian AJ, Holzbaur EL (2012) Dynactin is required for transport initiation from the distal axon. *Neuron* 74: 331 – 343

Nechipurenko IV, Berciu C, Sengupta P (2017) Centriolar remodeling underlies basal body maturation during ciliogenesis in *Caenorhabditis elegans*. *eLife* 6: e25686

Oberland S, Neuhaus EM (2014) Whole mount labeling of cilia in the main olfactory system of mice. *J Vis Exp* 94: e52299

O'Toole ET, McDonald KL, Mantler J, McIntosh JR, Hyman AA, Muller-Reichert T (2003) Morphologically distinct microtubule ends in the mitotic centrosome of *Caenorhabditis elegans*. *J Cell Biol* 163: 451 – 456

Ou G, Stuurman N, D'Ambrosio M, Vale RD (2010) Polarized myosin produces unequal-size daughters during asymmetric cell division. *Science* 330: 677 – 680

Pedersen LB, Veland IR, Schroder JM, Christensen ST (2008) Assembly of primary cilia. *Dev Dyn* 237: 1993 – 2006

Pelletier L, O'Toole E, Schwager A, Hyman AA, Muller-Reichert T (2006) Centriole assembly in *Caenorhabditis elegans*. *Nature* 444: 619 – 623

Perkins LA, Hedgecock EM, Thomson JN, Culotti JG (1986) Mutant sensory cilia in the nematode *Caenorhabditis elegans*. *Dev Biol* 117: 456 – 487

Pilling AD, Horiuchi D, Lively CM, Saxton WM (2006) Kinesin-1 and Dynein are the primary motors for fast transport of mitochondria in *Drosophila* motor axons. *Mol Biol Cell* 17: 2057 – 2068

Praitis V, Casey E, Collar D, Austin J (2001) Creation of low-copy integrated transgenic lines in *Caenorhabditis elegans*. *Genetics* 157: 1217 – 1226

Reck-Peterson SL, Yildiz A, Carter AP, Gennerich A, Zhang N, Vale RD (2006) Single-molecule analysis of dynein processivity and stepping behavior. *Cell* 126: 335 – 348

Reiter JF, Blacque OE, Leroux MR (2012) The base of the cilium: roles for transition fibres and the transition zone in ciliary formation, maintenance and compartmentalization. *EMBO Rep* 13: 608 – 618

Schouteden C, Serwas D, Palfy M, Dammermann A (2015) The ciliary transition zone functions in cell adhesion but is dispensable for axoneme assembly in *C. elegans*. *J Cell Biol* 210: 35 – 44

Schwarzenbacher K, Fleischer J, Breer H (2005) Formation and maturation of olfactory cilia monitored by odorant receptor-specific antibodies. *Histochem Cell Biol* 123: 419 – 428

Serwas D, Su TY (2017) Centrioles initiate cilia assembly but are dispensable for maturation and maintenance in *C. elegans*. *J Cell Biol* 216: 1659 – 1671

Shen Z, Zhang X, Chai Y, Zhu Z, Yi P, Feng G, Li W, Ou G (2014) Conditional knockouts generated by engineered CRISPR-Cas9 endonuclease reveal the roles of coronin in *C. elegans* neural development. *Dev Cell* 30: 625 – 636

Slevin LK, Romes EM, Dandulakis MG, Slep KC (2014) The mechanism of dynein light chain LC8-mediated oligomerization of the Ana2 centriole duplication factor. *J Biol Chem* 289: 20727 – 20739

Sonnichsen B, Koski LB, Walsh A, Marschall P, Neumann B, Brehm M, Alleaume AM, Artelt J, Bettencourt P, Cassin E, Hewitson M, Holz C, Khan M, Lazik S, Martin C, Nitzsche B, Ruer M, Stamford J, Winzi M, Heinkel R *et al* (2005) Full-genome RNAi profiling of early embryogenesis in *Caenorhabditis elegans*. *Nature* 434: 462 – 469

Sorokin S (1962) Centrioles and the formation of rudimentary cilia by fibroblasts and smooth muscle cells. *J Cell Biol* 15: 363 – 377

Strnad P, Leidel S, Vinogradova T, Euteneuer U, Khodjakov A, Gonczy P (2007) Regulated HsSAS-6 levels ensure formation of a single procentriole per centriole during the centrosome duplication cycle. *Dev Cell* 13: 203 – 213

Sulston JE, Horvitz HR (1977) Post-embryonic cell lineages of the nematode. *Caenorhabditis elegans*. *Dev Biol* 56: 110 – 156

Sulston JE, Schierenberg E, White JG, Thomson JN (1983) The embryonic cell lineage of the nematode *Caenorhabditis elegans*. *Dev Biol* 100: 64 – 119

Tabb DL, McDonald WH, Yates JR III (2002) DTASelect and Contrast: tools for assembling and comparing protein identifications from shotgun proteomics. *J Proteome Res* 1: 21 – 26

Tang Z, Lin MG, Stowe TR, Chen S, Zhu M, Stearns T, Franco B, Zhong Q (2013) Autophagy promotes primary ciliogenesis by removing OFD1 from centriolar satellites. *Nature* 502: 254 – 257

Tanos BE, Yang HJ, Soni R, Wang WJ, Macaluso FP, Asara JM, Tsou MF (2013) Centriole distal appendages promote membrane docking, leading to cilia initiation. *Genes Dev* 27: 163 – 168

Tateishi K, Yamazaki Y, Nishida T, Watanabe S, Kunimoto K, Ishikawa H, Tsukita S (2013) Two appendages homologous between basal bodies and centrioles are formed using distinct Odf2 domains. *J Cell Biol* 203: 417 – 425

Toller SV (1999) Assessing the impact of anosmia: review of a questionnaire's findings. *Chem Senses* 24: 705 – 712

Tsai JW, Bremner KH, Vallee RB (2007) Dual subcellular roles for LIS1 and dynein in radial neuronal migration in live brain tissue. *Nat Neurosci* 10: 970 – 979

Vorobjev IA, Chentsov Yu S (1982) Centrioles in the cell cycle. I. Epithelial cells. *J Cell Biol* 93: 938 – 949

Wang C, Li S, Januschke J, Rossi F, Izumi Y, Garcia-Alvarez G, Gwee SS, Soon SB, Sidhu HK, Yu F, Matsuzaki F, Gonzalez C, Wang H (2011) An ana2/ctp/mud complex regulates spindle orientation in *Drosophila* neuroblasts. *Dev Cell* 21: 520 – 533

Wang S, Moffitt JR, Dempsey GT, Xie XS, Zhuang X (2014) Characterization and development of photoactivatable fluorescent proteins for single-molecule-based superresolution imaging. *Proc Natl Acad Sci USA* 111: 8452 – 8457

Ward S, Thomson N, White JG, Brenner S (1975) Electron microscopical reconstruction of the anterior sensory anatomy of the nematode *Caenorhabditis elegans*. *J Comp Neurol* 160: 313 – 337

Ware RW, Clark D, Crossland K, Russell RL (1975) The nerve ring of the nematode *Caenorhabditis elegans*: sensory input and motor output. *J Comp Neurol* 162: 71 – 110

Wei Q, Zhang Y, Schouteden C, Zhang Y, Zhang Q, Dong J, Wonesch V, Ling K, Dammermann A, Hu J (2016) The hydrolethalus syndrome protein HYLS-1 regulates formation of the ciliary gate. *Nat Commun* 7: 12437

White JG, Southgate E, Thomson JN, Brenner S (1986) The structure of the nervous system of the nematode *Caenorhabditis elegans*. *Philos Trans R Soc Lond B Biol Sci* 314: 1 – 340

Williams CL, Li C, Kida K, Inglis PN, Mohan S, Semenec L, Bialas NJ, Stupay RM, Chen N, Blacque OE (2011) MKS and NPHP modules cooperate to establish basal body/transition zone membrane associations and ciliary gate function during ciliogenesis. *J Cell Biol* 192: 1023 – 1041

Xu T, Park SK, Venable JD, Wohlschlegel JA, Diedrich JK, Cociorva D, Lu B, Liao L, Hewel J, Han X, Wong CC, Fonslow B, Delahunty C, Gao Y, Shah H, Yates JR III (2015) ProLuCID: An improved SEQUEST-like algorithm with enhanced sensitivity and specificity. *J Proteomics* 129: 16 – 24

Ying G, Avasthi P, Irwin M, Gerstner CD, Frederick JM, Lucero MT, Baehr W (2014) Centrin 2 is required for mouse olfactory ciliary trafficking and development of ependymal cilia planar polarity. *J Neurosci* 34: 6377 – 6388

